Journal of Magnetism and Magnetic Materials 471 (2019) 432–438

Contents lists available at ScienceDirect

Journal of Magnetism and Magnetic Materials

journal homepage: www.elsevier.com/locate/jmmm

Research articles

Towards optimized MRI contrast agents for implant engineering: Clustering and immobilization effects of magnetic nanoparticles

Benedikt Mues[a,*], Eva M. Buhl[b], Thomas Schmitz-Rode[a], Ioana Slabu[a,*]

[a] Institute of Applied Medical Engineering, Helmholtz Institute, Medical Faculty, RWTH Aachen University, Germany
[b] Institute of Pathology, Electron Microscopy Facility, RWTH University Hospital Aachen, 52074 Aachen, Germany

ARTICLE INFO

Keywords:
Magnetic nanoparticles
Magnetic resonance imaging
MRI contrast agents
Magnetic nanoparticle agglomeration
Magnetic nanoparticle immobilization
Implants

ABSTRACT

Magnetic nanoparticles (MNP) have been successfully used as additives for the fabrication of implants such as hernia implants or vascular grafts in order to enable their in-vivo visualization with magnetic resonance imaging (MRI). However, functionality and long term stability of such implants were not quantitatively assessed until now. Reliable assessment of functionality is related not only to the determination of MNP concentration, but also to the impact of aggregation and immobilization of MNP inside the implant material on the MRI signal. In this regard, novel models must be developed which describe the relation between proton relaxation and both MNP clustering and mobility of MNP inside the implants. In this study, we experimentally quantify the transverse relaxation dependence on MNP size and MNP clusters, confirming theoretical descriptions. We identify three MNP size ranges for which different proton relaxation trends occur: One for which relaxivity increases with size (up to approx. 75 nm), a second for which relaxivity is constant (from 75 nm to 130 nm) and a third for which relaxivity decreases (from 130 nm to 220 nm). Further, we describe the impact of gradual MNP immobilization in agarose gels on relaxivity for three MNP types representing either of the identified size ranges. For all MNP types, we observe an increase of relaxivity with agarose content up to an MNP type specific maximum value. The relative rise of relaxivity is higher for MNP with larger sizes. The highest increase of the transverse relaxivity from 240 $mM^{-1}s^{-1}$ to 1000 $mM^{-1}s^{-1}$ is achieved for MNP clusters after immobilization in a gel with 7%(w/w) agarose. The effects of MNP clustering and immobilization on relaxivity are valuable information for the engineering of implants with different contrast properties in MRI. Further, the relation between MNP immobilization and relaxivity values may serve as a basis for future non-invasive assessment of changes in implant functionality by MRI measurements.

1. Introduction

Magnetic nanoparticles (MNP) have been investigated as contrast agents in magnetic resonance imaging (MRI) for very promising applications such as tumor imaging, cell labelling and tissue engineering [1–4]. In order to monitor with MRI the postoperative location and structure of implants, e. g. hernia implants, MNP have been used as additives. Due to their contrast agent properties, MNP enable a non-invasive visualization of implants with MRI. Such implants were already clinically tested and are currently available on the market [5]. Usually most of the textile materials used for implant engineering cannot be imaged with conventional radiology imaging techniques. By incorporation of MNP inside the implant material, the implants can be then visualized with MRI. The incorporated MNP influence the relaxation properties of water protons in their surroundings and enable the visualization of the whole implant [4,6–9]. Local changes in the implant structure which could cause implant failure are related to varying local MNP concentrations. In this regard, quantitative methods such as MR relaxometry can be used to determine the local MNP concentration [10]. The MNP effect on proton relaxation of water molecules is described by the MNP ability to shorten the protons relaxation time which results in a signal loss. The relaxivity r_2 is the proportionality factor between the inverse relaxation time, i.e. the relaxation rate $R_2 = 1/T_2$, and the MNP concentration. However, relaxivity is not only dependent on the MNP concentration but also on MNP properties. A strong dependency of relaxivity on size and agglomeration state of in water dispersed MNP was theoretically described and validated with experimental measurements before [11–14]. According to theory, three

* Corresponding authors at: Institute of Applied Medical Engineering, Helmholtz Institute, Pauwelsstrasse 20, 52072 Aachen, Germany (Benedikt Mues). Institute of Applied Medical Engineering, Helmholtz Institute, Pauwelsstrasse 20, 52072 Aachen, Germany (Ioana Slabu).
E-mail addresses: mues@ame.rwth-aachen.de (B. Mues), slabu@ame.rwth-aachen.de (I. Slabu).

https://doi.org/10.1016/j.jmmm.2018.09.119
Received 24 June 2018; Received in revised form 7 September 2018; Accepted 28 September 2018
Available online 29 September 2018
0304-8853/

different MNP size ranges exist for which relaxivity behaves differently: in the first size range, defined by MNP with smaller sizes (up to approx. 75 nm), relaxivity increases for increasing diameters, in the second size range (from 75 nm to 130 nm), relaxivity shows a constant maximum value, whereas in the third size range (greater than approx. 130 nm), relaxivity decreases again. An additional effect to that of size-dependent behavior of relaxivity arises from the immobilization state of the MNP. This effect is relevant for MNP immobilized in different implant materials, especially in the biodegradable materials, which have different stiffness properties for different degradation states. In such cases, the MNP mobility is partially or fully blocked. Consequently, for the quantification of local MNP concentration inside implants with MRI and for the determination of implant functionality, it is crucial to analyze the impact of MNP mobility on relaxivity.

Considering the proton relaxation mechanisms in MRI in presence of MNP, we expect that MNP immobilization influences the magnetic moment relaxation of the protons, more precisely their dephasing behavior. For the case of freely dispersed MNP in water, protons of water molecules diffuse rapidly in the area of local field inhomogeneities caused by the MNP magnetization, experiencing thus a broad range of fast changing magnetic fields. This leads to slower dephasing of the proton magnetic moments compared to the one for inhibited proton diffusion [15,16]. Such situations can occur for water protons and MNP immobilized inside the material of implants, where the diffusion of water protons and the MNP mobility is inhibited. In this way, the fluctuation of the magnetic fields experienced by protons decreases leading to a faster dephasing of the proton magnetic moments. A faster dephasing ends in an increase of relaxivity.

In the present work, the dependence of relaxivity on gradual MNP immobilization for MNP with different sizes is analyzed. For that, monodispersed MNP and MNP clusters with different hydrodynamic sizes were synthesized and their relaxivity values were measured with a clinical 3 T MRI scanner. Three different MNP types, Resovist®, self-synthesized MNP and MNP clusters, belonging to different categories of theoretically predicted relaxation mechanisms, were then chosen for further investigation of the MNP immobilization effect on relaxivity. Each of the three MNP types was gradually immobilized in hydrogels of low melt agarose and the relaxivity was determined by relaxation measurements.

2. Material and methods

2.1. Materials

For the synthesis of the MNP, the chemicals iron(III) chloride hexahydrate ($FeCl_3{\cdot}6H_2O$, p.a., Sigma-Aldrich), iron(II) chloride tetrahydrate ($FeCl_2{\cdot}4H_2O$, p.a., Sigma-Aldrich), iron(II) sulfate heptahydrate ($FeSO_4{\cdot}7H_2O$, p.a., Sigma-Aldrich), sodium nitrite ($NaNO_2$, p.a., Sigma-Aldrich) ammonium hydroxide (NH_4OH, ACS reag., Sigma-Aldrich) and lauric acid ($C_{12}H_{24}O_2$ > 98%, FCC, Sigma-Aldrich) were used. For the synthesis of the of the MNP clusters, PLGA (85:15 lactide/glycolide, M_W 150 kDa) was purchased from Purasorb® and polyvinyl alcohol (PVA, M_W 31–50 kDa, 98–99% hydrolyzed) as well as chloroform was purchased from Sigma-Aldrich. Low melt agarose (LMA, Carl Roth) was used to prepare the MRI gel phantoms. Further, Resovist® (Bayer Schering AG. Germany) iron oxide nanoparticles with a carboxydextran coating were used.

2.2. Synthesis of magnetic nanoparticles

To obtain lauric acid coated iron oxide magnetite (Fe_3O_4) nanoparticles (MNP) with different hydrodynamic sizes a oxidative precipitation method of $FeSO_4$ and $NaNO_2$ in presence of a base was used [17]. Various molar ratios of Fe^{2+}/NO^{2-} of 3/1, 5/1, 6/1, 7/1, 10/1, 12/1, 24/1, 30/1 were tested. For this, 1.5 g $FeSO_4$ and the corresponding content $NaNO_2$ were dissolved in 9 ml of deionized water and heated up to 40 °C in a water bath. Subsequently, 5 ml of NH_4OH were added dropwise under constant stirring. After the precipitation was completed, the solution was stirred for 30 min at room temperature. The precipitated colloidal MNP were washed ten times with 60 ml of a 0.7 M NH_4OH solution to remove the sulfate and nitrite ions. For the coating, the solution with precipitated MNP was heated up in an oil bath at 90 °C. Then, 0.2 g lauric acid was added under constant stirring. The resulting MNP suspension was cooled down to room temperature and centrifuged for 10 min at 500 rpm with a Rotina 420R Centrifuge (Thermo Scientific, USA).

2.3. Synthesis of magnetic nanoparticle clusters

Magnetic nanoparticle clusters were prepared by a double emulsion technique based on the methods described in [18,19]. First, iron oxide magnetite (Fe_3O_4) nanoparticles were synthesized *via* the co-precipitation of Fe^{2+} and Fe^{3+} ions (molar ratio Fe^{2+}/Fe^{3+} of 1/2) in the presence of a base [20]. 8 g $FeCl_3$ and 4 g $FeCl_2$ were dissolved in 33.7 ml deionized water. Subsequently, 16.7 ml of NH_4OH were added dropwise under constant stirring at room temperature. Next, the solution maintained under vigorous stirring for 30 min. The precipitated MNP were washed several times to remove the chloride ions. For the coating, the resulting MNP suspension was heated up in an oil bath at 90 °C and 1.5 g lauric acid were added under constant stirring. The MNP suspension was cooled down to room temperature and centrifuged for 10 min at 4500 rpm with a Rotina 420R Centrifuge (Thermo Scientific, USA). This particle system of lauric acid coated MNP (in the following denotes as LANP) is the precursor for the following cluster generation.

For the synthesis of MNP clusters, the lauric acid coated MNP were embedded in PLGA. For this, 20 mg of PLGA were dissolved in 3 ml chloroform. Subsequently, 1 ml of the MNP suspension with an iron concentration of 10 mg(Fe)/ml was emulsified in the chloroform solution by sonication at 80 W for 1 min with an ultrasonic homogenizer (Bandelin, Germany) forming a water-in-oil emulsion (W_1/O). Then, 8 ml of 3%(w/v) PVA solution (W_2) was added to the emulsion and sonicated for 1 min at the same conditions as before. The obtained double emulsion water-in-oil-in-water ($W_1/O/W_2$) was diluted into 10 ml of 3%(w/v) PVA solution under constant stirring. Afterwards, the chloroform was removed using a rotation evaporator (Heidolph, Germany) with 90 rpm, at 40 °C and 430 mbar. Next, the remaining solution was centrifuged for 10 min at 4500 rpm with a Rotina 420R Centrifuge (Thermo Scientific, USA). The magnetic MNP clusters (in the following denotes as LANP@Cluster) were obtained *via* magnetophoresis from PLGA particles without MNP.

2.4. Preparation of the agarose hydrogels

In order to realize different immobilization states of the MNP and MNP clusters, hydrogels containing various LMA monomer mass fractions of f = (0.1, 0.3, 0.5, 1.0, 1.5, 2.0, 3.0… 10.0) %(w/w) were prepared. For that, LMA was mixed with deionized water and MNP or MNP clusters. The mixture was heated up to 80 °C for 30 min and was vortexed several times ending in a homogenous distribution of LMA and MNP or MNP clusters. The pore size d_{pore} of the resulting gels dependents on the LMA content and can be estimated using relations from literature as follows [21]: $d_{pore} = a{\cdot}f^{-\gamma}$ with a = 563.6 nm and γ = 0.62.

2.5. Basic characterization

The hydrodynamic diameters d_{hyd} were measured by dynamic light scattering (DLS) using a Zetasizer Nano S (Malvern Instruments Ltd., United Kingdom) at a wavelength of λ = 633 nm (detection angle of 173°). All measurements were performed with MNP diluted in deionized H_2O at 20 °C and repeated three times. The mean hydrodynamic size was obtained by fitting the log-normal distribution probability density function (see Appendix A, equation. (A.1)) to the measured

intensity data.

The core diameters d_C of the MNP and the MNP clusters were investigated *via* transmission electron microscopy (TEM) with a Zeiss LEO 906 microscope (Carl Zeiss GmbH, Germany) operated at 60 kV. For that, 1 µl of the sample was pipetted on formvar-carbon-coated nickel grids (200 mesh) (Electron Microscopy Sciences, USA) and air-dried under ambient conditions. The core diameter of about 150 MNP for each for the synthesized MNP types was measured using the software GIMP and fitted with the cumulative log-normal distribution probability density function (see Appendix A, equation. (A.2)).

The samples were magnetically characterized using a SQUID magnetometer MPMS 5S (LOT Quantum Design, USA). For the preparation, 30 µl of the sample were mixed with 30 µl 15%(w/w) mannitol solution in a polycarbonate (PC) capsule and freeze dried at -85 °C and 0.04 mbar in a lyophilisator (Alpha 2–4 LDplus, Germany) for 12 h. For the determination of the saturation magnetization values, magnetization measurements were performed at 295 K varying the field strength from zero to $4{\cdot}10^6$ A/m. From the fit with the Langevin function (see Appendix B, equation (B.1)), the saturation magnetization M_S was determined. The ZFC magnetization curves were obtained by measuring the magnetization in a magnetic field of 796 A/m while the temperature was stepwise increased from 5 K to 295 K. The FC magnetization curves were obtained by magnetization measurements executed in the same field as for ZFC measurements while the temperature was stepwise decreased to 5 K.

Magnetic resonance measurements were performed using a clinical 3 T Achieva MRI Scanner (Philips Healthcare, The Netherlands). For excitation and signal reception a body coil SENSE XL Torso Coil 4535–673-94943 (Philips, Healthcare, The Netherlands) was used. Each sample was investigated for 8 different iron concentrations [Fe] up to 0.2 mM. The samples (MNP dispersed in water or in agarose gels) were embedded inside a polyacrylic acid gel phantom as described in ASTM standards [22] and measured with a Turbo Spin Echo (TSE) sequence (TR = 1500 ms, 32 echoes, echoes of the echo train TE = [10, 20, …, 320] ms, FOV = 366 x 366 mm, matrix 512 × 512, slice thickness 3 mm, flip angle 90°). This sequence was chosen after multiple testing of appropriate TEs and TRs for the best signal acquisition. From these measurements, the transverse relaxivity $r_2 = (R_2 - R_{2,0})/[\mathrm{Fe}]$, with R_2 the relaxation rate of the MNP sample and $R_{2,0}$ the relaxation rate of the solvent, was calculated using Matlab (The MathWorks Inc., USA).

3. Results and discussion

3.1. Dependency of transverse relaxivities on MNP hydrodynamic size

The transverse relaxivities of the MNP in dependence of their hydrodynamic sizes are shown in Fig. 1. Here, MNP clusters are treated as particles with bigger size. All samples were dispersed in deionized water and their hydrodynamic size was checked before each measurement to account for the changes in size due to instabilities. Detailed characterization of these MNP is provided in the Supplementary Information Table S.1. The behavior of relaxivity with increasing hydrodynamic sizes shown in Fig. 1 is in line with the theoretical predictions of the protons outer sphere relaxation theory as described in the following.

The outer sphere relaxation theory predicts the influence of MNP with different sizes on the protons transverse relaxation and was proven by experiment [13,23]. The transverse relaxivity dependence on MNP size is classified in three regimes: the motional averaging regime (MAR), the static dephasing regime (SDR) and the echo limiting regime (ELR) [11,24]. In the MAR, the proton diffusion length is larger than the characteristic length of the magnetic field disturbance caused by the MNP. Water protons diffuse rapidly around the MNP, thus experiencing a broad range of fast changing magnetic fields, which are effectively cancelled in the time-average. In the MAR, the theory predicts a quadratic relaxivity rise with MNP size [24]. As the MNP diameter

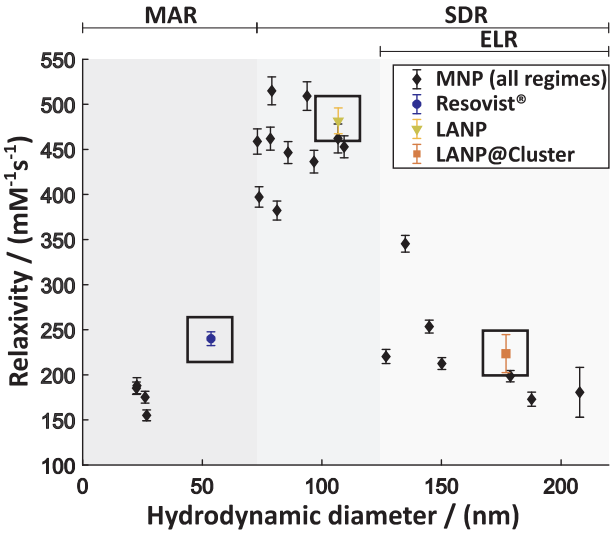

Fig. 1. Transverse relaxivity values for MNP with different hydrodynamic diameters between 22.7 nm and 220 nm. The measured values fit the theoretical predictions of the regimes MAR, SDR and ELR as indicated. One exemplary particle type in each regime is highlighted. These particles are chosen for further investigations (see section 3.3).

increases, water protons will reach a small diffusion length compared to the MNP size. Then, they experience non-averaged variations in local magnetic fields (quasi-static local magnetic fields) causing quicker relaxation of the proton magnetic moments, i. e. increased relaxivity. Above a certain MNP diameter, the SDR regime is reached, in which relaxivity first shows multiple plateaus having different magnitudes that are attributed to different saturation magnetization values of the MNP. For ever higher MNP diameters, relaxivity decreases with MNP size due to partial refocusing of the proton magnetic moments in the strong gradients of the quasi-static magnetic fields caused by the MNP (ELR subregime of SDR, in the following denoted as ELR/SDR). Protons sufficiently close to the MNP will experience gradients so strong that they will be rapidly dephased. These protons cause prompt signal decay that is unobservable with MRI techniques. According to the partial refocusing model presented by Gillis et al. [24], spatial separation exists between an inner region where the gradients are too strong for the refocusing pulses to be efficient and an outer region where they are efficient. Due to the big hydrodynamic MNP sizes realized by a thick MNP coating, the distance of the outer region water protons to the magnetic core of the MNP is getting so large that the refocusing pulse starts to be effective as described by the partial refocusing model. Here, the echo time TE of the MRI sequence plays an important role: For increasing TE, the contribution from the inner region will become larger and larger.

In earlier publications, the MAR was identified for MNP sizes up to approx. 80 nm, SDR for 80 nm to 100 nm and the ELR/SDR for sizes above 100 nm [23]. The MNP in this work were synthesized with sizes between 23 nm and 188 nm (see section 2.2) to span the entire size range of all regimes (see Supplementary Information Table S.1). In Fig. 1 the three different regimes can be identified. For the first regime (MAR) r_2 increases with particle diameter (up to approx. 75 nm). Resovist® (d_{hyd} = 54 nm, see Fig. 1) can be clearly assigned to the MAR regime [24,25]. The MNP type in Fig. 1 denoted as LANP (d_{hyd} = 107 nm) fits to the SDR regime which spans the size range from 75 nm to 220 nm and where the relaxivity values show several plateaus. The r_2 plateaus arise due to different saturation magnetization values (see Supplementary Information Table S.1) which is in line with the findings in literature [23]. The particle type LANP@Cluster (d_{hyd} = 176 nm) (see Fig. 1) belongs to the ELR/SDR regime in which r_2 decreases with increasing MNP diameter (d_{hyd} > 120 nm). Precise

Table 1
Particle properties: d_C denotes the core diameter, d_{hyd} the hydrodynamic diameter, M_S the saturation magnetization and r_2 the transverse relaxivity for the MNP dispersed in water.

MNP	d_C [nm]	d_{hyd} [nm]	M_S [Am^2/kg(Fe)]	r_2 [mM^{-1}s^{-1}] in H_2O
Resovist®	6.0 ± 1.7	53.6 ± 4.3	72.9 ± 0.8 [27]	240.1 ± 7.7
LANP	10.2 ± 2.4	106.8 ± 7.7	99.4 ± 0.8	481.6 ± 14.4
LANP@Cluster	98.7 ± 18.4	176 ± 6.0	101.0 ± 0.6	223.5 ± 21.1

delineation between the three regimes remains challenging especially due to MNP size distribution. It was shown that for MNP with a broad size distribution, the particles with smaller sizes have a stronger influence on relaxivity than the bigger ones [26]. Nevertheless, Resovist®, LANP and LANP@Cluster can be clearly identified as exemplary particle types representing the three regimes. These are chosen for further investigations of the effect of particle immobilization on relaxivity.

3.2. Basic characteristics of immobilized MNP

The properties of the three MNP types Resovist®, LANP and LANP@Cluster representing the three relaxation regimes are summarized in Table 1.

Fig. 2 displays exemplary TEM images for Resovist®, LANP and LANP@Cluster. In Fig. 2b the LANP particles are shown. The LANP particles were used for preparation of the LANP@Cluster (Fig. 2c). From the fit with the cumulative density function (Fig. 3), the average core diameter d_C was calculated. Resovist® shows the smallest core diameter of approx. 6 nm which is consistent with the findings in literature [28]. LANP@Cluster have a core diameter of approx. 99 nm, which is about ten times larger than the one of the LANP particles (about 10 nm).

Fig. 4 displays the DLS measurements for Resovist®, LANP and LANP@Cluster. The hydrodynamic diameters d_{hyd} were determined from the PDF fit to the size distribution data. The LANP are approximately twice as big as Resovist® and half as much in size compared to the LANP@Cluster.

Magnetic measurements were carried out for the samples LANP and the LANP@Cluster. The magnetization value for LANP@Cluster is smaller (Fig. 5a) compared to the one of LANP especially at low magnetic fields. Furthermore, the peak of the ZFC curve (Fig. 5b) is shifted towards higher temperatures for the LANP@Cluster. Both, the lower magnetization and the shift of the ZFC peak, can be attributed to demagnetizing dipole–dipole interactions between the MNP inside the LANP@Cluster [29,30]. The saturation magnetization of about 100 Am^2/kg(Fe) is nearly the same for LANP and LANP@Cluster (Tab. 1). A smooth increase of the magnetization at high fields for the LANP is present. The Langevin function used to fit the data has therefore a linear correction. This high field magnetization linear increase has been often attributed to MNP surface spin canting effects [31].

3.3. Transverse relaxivities of immobilized MNP

In order to investigate relaxivity changes due to particle immobilization in each regime, Resovist®, LANP and LANP@Cluster were chosen as representative MNP for the MAR, SDR and ELR/SDR regime, respectively. Each of these particle types were embedded in hydrogels with different low melt agarose content of up to 10%(w/w) and with different iron concentrations (see section 2.5).

Fig. 6a shows for each particle type, that relaxivity increases with agarose content up to a particle type specific maximum value and then decreases. Although starting from almost the same relaxivity value of approx. 240 mM^{-1} s^{-1}, Resovist® particles show a moderate increase up to a maximum of 615 mM^{-1} s^{-1} at 8%(w/w) agarose, while LANP@Cluster particles already reach this value at 0.5%(w/w) agarose. Having reached its maximum at 8%(w/w) agarose, the relaxivity of Resovist® decreases slightly to 540 mM^{-1} s^{-1} at 10%(w/w) agarose. For LANP@Cluster, a major increase of the relaxivity from 223 mM^{-1} s^{-1} to 453 mM^{-1} s^{-1} occurs at only 0.1%(w/w) agarose. The relaxivity of LANP@Cluster increases further until the maximum of approx. 1000 mM^{-1} s^{-1} is reached at 8%(w/w) agarose. LANP particles show the highest relaxivity compared to Resovist® and LANP@Cluster when they are freely dispersed in water. In agarose gels, the LANP relaxivity strongly increases with agarose content up to 3%(w/w) agarose followed by a slight increase from 700 mM^{-1} s^{-1} to its maximum value of 750 mM^{-1} s^{-1} at 6%(w/w) agarose. Having reached their specific maximum value, relaxivity decreases for all particles types, showing a much steeper decrease for LANP and LANP@Cluster compared to the one for Resovist®: For LANP@Cluster, a relaxivity decrease by 40% to 570 mM^{-1} s^{-1} and for LANP a relaxivity decrease by 60% to 300 mM^{-1} s^{-1} is observed.

To explain these findings, the outer sphere relaxation theory described in section 3.1 is appropriate. Gels with higher agarose content show higher viscosity which leads to inhibited proton diffusion [32,33]. In case of small agarose fractions, the diffusion of the water protons as well as the mobility of the particles is not completely blocked so that the protons still experience fluctuating magnetic fields. The relaxation increase for Resovist® particles can therefore be explained as follows: With increasing agarose content the water protons diffusion is slower causing a quicker dephasing of the proton magnetic moments which consequently leads to an increase of relaxivity. The protons experience steadily decreasing fluctuation of magnetic fields which causes a

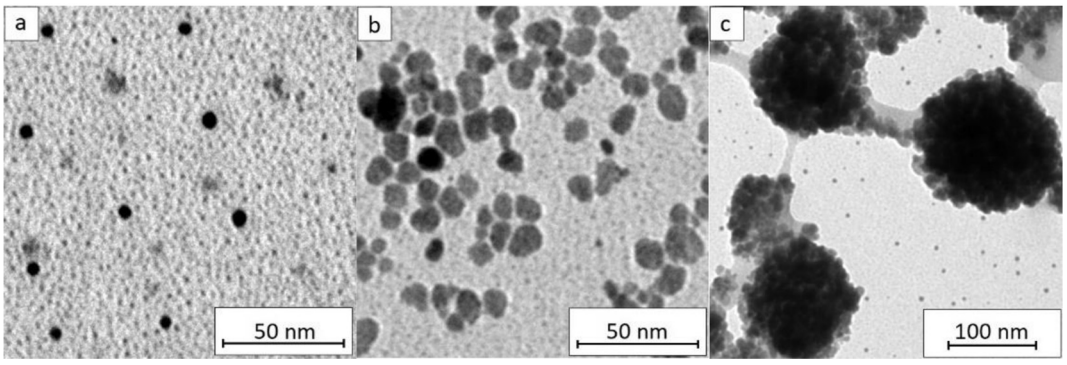

Fig. 2. TEM images of (a) Resovist®, (b) lauric acid coated magnetic nanoparticles (LANP) and (c) cluster LANP@Cluster.

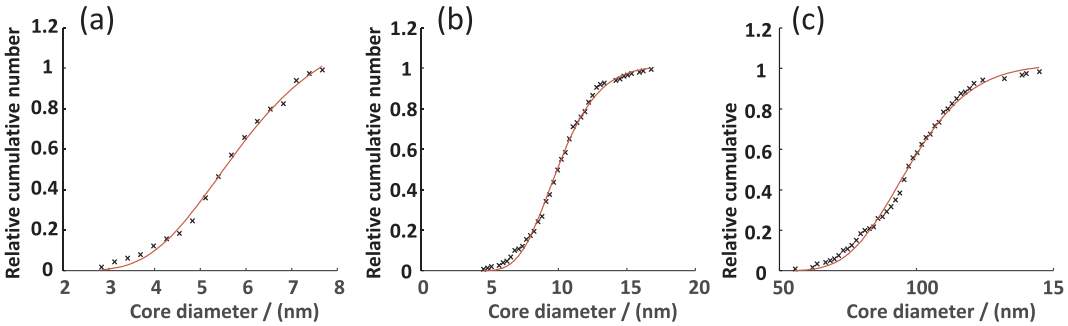

Fig. 3. Core diameter distribution with a fit to a log-normal CDF of (a) Resovist®, (b) lauric acid coated magnetic nanoparticles (LANP) and (c) cluster LANP@Cluster.

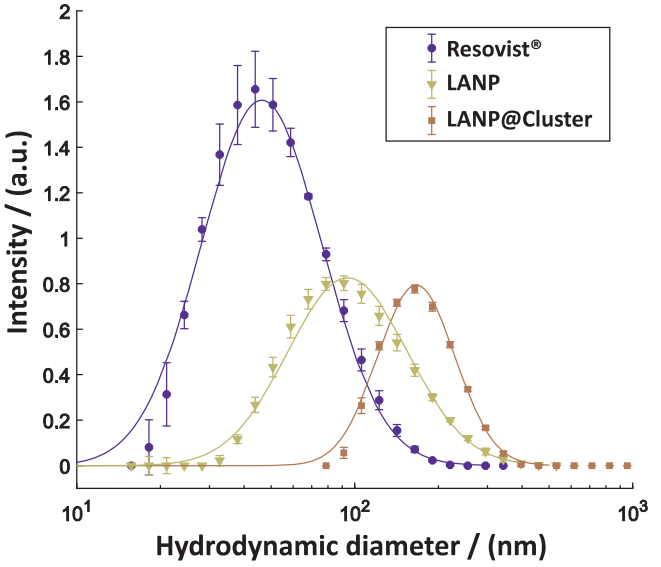

Fig. 4. Intensity size distribution of the hydrodynamic diameters of Resovist®, LANP and LANP@Cluster with a fit to the PDF of a log-normal distribution.

relaxivity increase analog to the one of the MAR regime (see section 3.1). This behavior dominates up to the maximum relaxivity value at 8%(w/w) agarose.

For both particles types LANP and LANP@Cluster, the partially inhibited proton diffusion leads to increased relaxivity values. This increase is similar for both particle types at low agarose content. Above 3%(w/w) agarose, the LANP@Cluster show steeper relaxivity increase compared to the one of the LANP. Since LANP and LANP@Cluster particles have almost the same saturation magnetization, the difference in relaxivity increase of the LANP and compared to the LANP@Cluster is not due to different magnetic properties and has to be attributed to different immobilization states of the particles. The increase of the agarose content results in smaller hydrogel pore sizes leading to a stronger immobilization of bigger particles than of smaller ones at the same agarose content [21,34]. Such a situation is illustrated in Fig. 7 for two exemplary immobilization states of LANP and LANP@Cluster in a hydrogel with a small and high amount of agarose resulting in large and small mesh sizes of the hydrogel, respectively. For a small amount of agarose, loose saccharide chains are not able to immobilize LANP or LANP@Cluster, so these loose chains only have an effect on water proton diffusion (see Fig. 7a and c). Increasing the amount of agarose leads to clearly defined pore sizes in which the particle immobilization is considerably higher for the LANP@Cluster (see Fig. 7d) than for the LANP particles (see Fig. 7b). Analog to the SDR regime, the stronger inhibition of the LANP@Cluster mobility leads to an even lower fluctuation of magnetic fields experienced by the water protons causing a faster dephasing of their magnetic moments. This results in higher relaxivity values.

The observed relaxivity increase in relation to the corresponding pore size of the gels is depicted in Fig. 6b. The relaxivity maximum for the LANP@Cluster is reached at a pore size of 170 nm which matches their hydrodynamic diameter (about 176 nm). The particles Resovist® and LANP have lower relaxivity values, probably due to their smaller sizes and lower immobilization states. Furthermore, Resovist® shows relatively small relaxivity values in the whole immobilization range which can be attributed to the lower saturation magnetization of 73 $Am^2/kg(Fe)$ compared to approx. 100 $Am^2/kg(Fe)$ for the other particle types. Because of different structures and chains in the agarose gels, a precise functional relation between agarose content and pore size does not exist, so the attribution of the agarose content to a certain

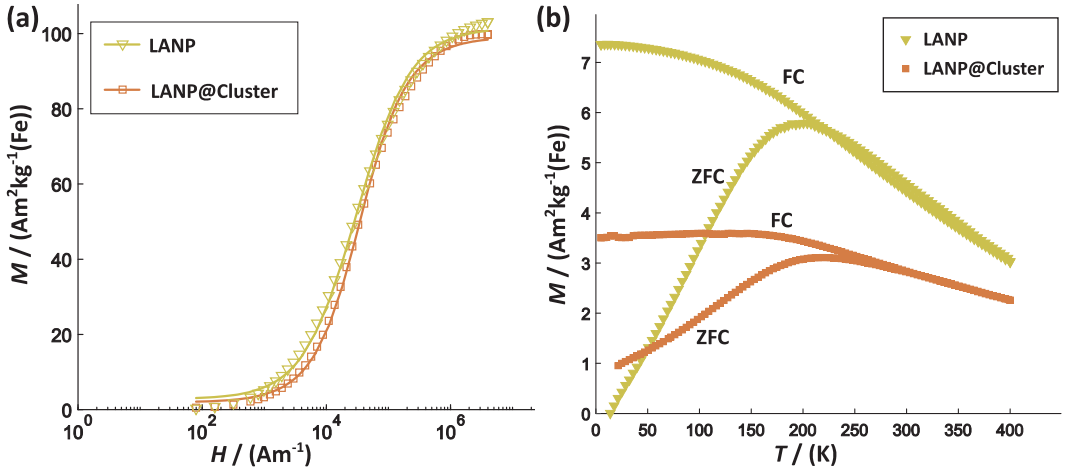

Fig. 5. (a) Magnetization with the Langevin function fitted curves for LANP and LANP@Cluster. (b) ZFC and FC magnetization curves of LANP and LANP@Cluster.

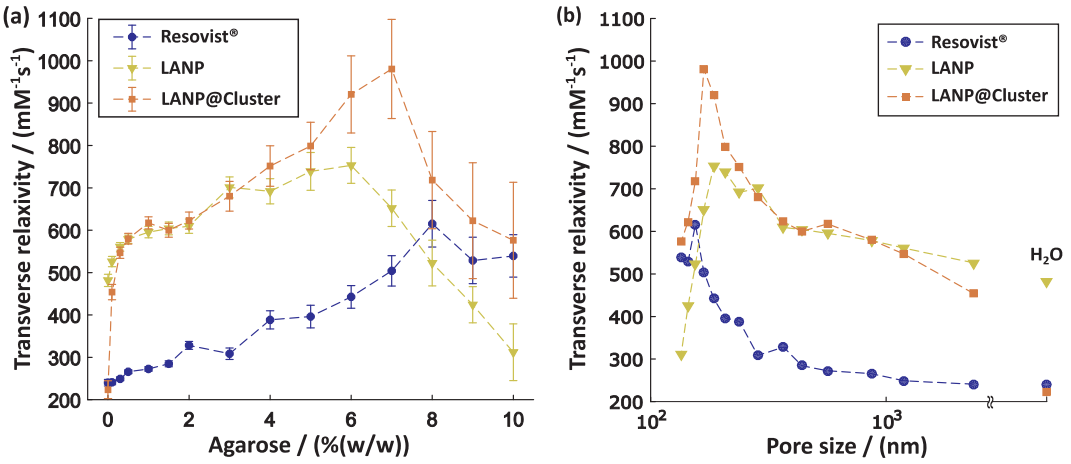

Fig. 6. Transverse relaxivity values for gradually immobilized particle systems Resovist®, LANP and LANP@Cluster belonging to the regimes MAR, SDR and ELR/SDR, respectively. (a) Transverse relaxivity versus the mass fraction of low melt agarose in the hydrogel. (b) Transverse relaxivity versus pore size of the different agarose gels. In (b) only the nominal values are given.

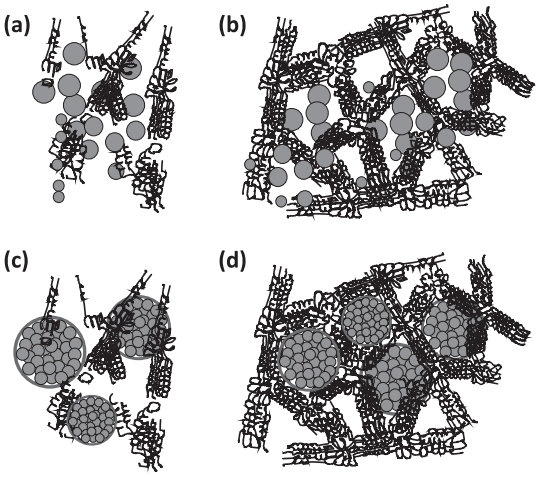

Fig. 7. Graphical illustration of LANP and LANP@Cluster immobilized in gels for two exemplary amounts of agarose (small and high) of the hydrogel: (a) LANP particles inside the hydrogel with small and (b) with high amount of agarose. (c) LANP@Cluster inside the hydrogel for the same small and (d) high amount of agarose.

immobilization state of MNP is difficult. Nevertheless, the relation between relaxivity and particle immobilization state is obvious and is line with findings in literature. Paquet et al. reported an increase of the relaxivity values for MNP with stronger binding of water protons inside the MNP hydrogel coating [26].

The fast decrease of relaxivity at higher amount of agarose could be explained with the partial refocusing model [24]: Due to abundance of saccharide chains and particles in the hydrogel, proton diffusion as well as MNP mobility are strongly inhibited leading strong magnetic field gradients close to the MNP. The proton magnetic moment will then be rapidly dephased. Analog to the trend in the ELR/SDR regime, these protons would cause prompt signal decay that is unobservable with MRI techniques. However, protons with a larger distance to MNP can be partially refocused which results in a non-zero effective relaxivity which decreases with increasing immobilization. We assume that this relaxivity also dependents on the used echo time TE in the MRI experiment. However, this assumption must be proved in future experiments.

4. Conclusions

Using MNP with different hydrodynamic sizes as contrast agents, we experimentally investigated the transverse relaxivity dependence on MNP size and MNP clusters confirming theoretical descriptions of the three relaxation regimes MAR, SDR and ELR/SDR. Further, in order to mimic the relaxation behavior of MNP embedded in implants, MNP with hydrodynamic sizes of about 50 nm, 100 nm and 200 nm representing the three above-mentioned regimes were immobilized in hydrogels with different agarose contents. In this way, different immobilization states of the MNP were obtained. The results show that immobilization first has an enhancing effect on relaxivity independent of which regime the MNP belong to. For increasing agarose contents, the relaxivity of each particle system increases up to a certain particle type specific maximum value and then decreases. The highest relaxivity value of approx. $1000\,mM^{-1}s^{-1}$ was achieved for clustered particles. This is explained by stronger immobilization of the cluster in agarose with gradually decreasing pore sizes of the hydrogel for which the water protons experience a strong gradient of the quasi-static magnetic field generated by the MNP clusters. The effects of MNP clustering and immobilization on the transverse relaxivity are valuable information for the engineering of future implants with different contrast properties in MRI. Further, relaxivity dependence on MNP immobilization might be a useful basis for non-invasive assessment of changes in implant functionality with MRI measurements.

5. Declaration of interest

None.

Appendix

A: Log-normal distribution probability density function

The log-normal distribution probability density function (PDF) is defined as

$$\mathrm{PDF}(d,\mu,\sigma) = \frac{1}{\sqrt{2\pi}\cdot d\cdot\sigma}\cdot\exp\left(-\frac{(\ln(d)-\mu)^2}{2\sigma^2}\right), \quad (A.1)$$

and the cumulative distribution function (CDF) is defined as

$$\mathrm{CDF}(d, \mu, \sigma) = \frac{1}{2} + \left(1 + \mathrm{erf}\left(\frac{\ln(d) - \mu}{\sqrt{2\sigma}}\right)\right), \tag{A.2}$$

with the parameters, μ and σ, from which the mean and variance are calculated with $d_C = \exp(\mu + \sigma^2/2)$ and $\sigma_{d_C}^2 = \exp(2\mu + \sigma^2)\cdot(\exp(\sigma^2) - 1)$, respectively.

B: Langevin function

The Langevin function is defined as

$$L(\xi) = \coth(\xi) - \frac{1}{\xi}, \tag{B.1}$$

with $\xi = \mu H/(k_B T)$ where $\mu = V_M M_S$ denotes the particle magnetic moment. Here, M_S is the saturation magnetization, V_M the mean magnetic volume, H the applied magnetic field and $k_B = 1.38 \cdot 10^{-23}$ J/K the Boltzmann constant.

Appendix A. Supplementary data

Supplementary data to this article can be found online at https://doi.org/10.1016/j.jmmm.2018.09.119.

References

[1] Z. Shen, A. Wu, X. Chen, Iron oxide nanoparticle based contrast agents for magnetic resonance imaging, Mol. Pharmaceut. 14 (2017) 1352–1364, https://doi.org/10.1021/acs.molpharmaceut.6b00839.

[2] H. Liu, J. Zhang, X. Chen, X.-S. Du, J.-L. Zhang, G. Liu, W.-G. Zhang, Application of iron oxide nanoparticles in glioma imaging and therapy: from bench to bedside, Nanoscale 8 (2016) 7808–7826, https://doi.org/10.1039/C6NR00147E.

[3] K. Andreas, R. Georgieva, M. Ladwig, S. Mueller, M. Notter, M. Sittinger, J. Ringe, Highly efficient magnetic stem cell labeling with citrate-coated superparamagnetic iron oxide nanoparticles for MRI tracking, Biomaterials 33 (2012) 4515–4525, https://doi.org/10.1016/j.biomaterials.2012.02.064.

[4] S. Zhou, R. Yang, Q. Zou, K. Zhang, T. Yin, W. Zhao, J.G. Shapter, G. Gao, Q. Fu, Fabrication of tissue-engineered bionic urethra using cell sheet technology and labeling by ultrasmall superparamagnetic iron oxide for full-thickness urethral reconstruction, Theranostics 7 (2017) 2509–2523, https://doi.org/10.7150/thno.18833.

[5] Dyna Mesh Tailored Implants made of PVDF, 2018. https://en.dyna-mesh.com/visible-gb/ (accessed August 28.08.18).

[6] M.E. Mertens, S. Koch, P. Schuster, J. Wehner, Z. Wu, F. Gremse, V. Schulz, L. Rongen, F. Wolf, J. Frese, V.N. Gesché, M. van Zandvoort, P. Mela, S. Jockenhoevel, F. Kiessling, T. Lammers, USPIO-labeled textile materials for non-invasive MR imaging of tissue-engineered vascular grafts, Biomaterials 39 (2015) 155–163, https://doi.org/10.1016/j.biomaterials.2014.10.076.

[7] M.E. Mertens, A. Hermann, A. Bühren, L. Olde-Damink, D. Möckel, F. Gremse, J. Ehling, F. Kiessling, T. Lammers, Iron oxide-labeled collagen scaffolds for non-invasive mr imaging in tissue engineering, Adv. Funct. Mater. 24 (2014) 754–762, https://doi.org/10.1002/adfm.201301275.

[8] I. Slabu, G. Guntherodt, T. Schmitz-Rode, M. Hodenius, N. Kramer, H. Donker, G.A. Krombach, J. Otto, U. Klinge, M. Baumann, Investigation of superparamagnetic iron oxide nanoparticles for mrvisualization of surgical implants, Curr. Pharmaceut. Biotechnol. 13 (2012) 545–551.

[9] I. Slabu, N. Wirch, T. Caumanns, R. Theissmann, M. Krüger, T. Schmitz-Rode, T.E. Weirich, Electron tomography and nano-diffraction enabling the investigation of individual magnetic nanoparticles inside fibers of MR visible implants, 315303, J. Phys. D Appl. Phys. 50 (2017), https://doi.org/10.1088/1361-6463/aa77e8.

[10] A.A.O. Carneiro, G.R. Vilela, D.B. de Araujo, O. Baffa, MRI relaxometry: methods and applications, Braz. J. Phys. 36 (2006) 9–15.

[11] A. Roch, Y. Gossuin, R.N. Muller, P. Gillis, Superparamagnetic colloid suspensions: Water magnetic relaxation and clustering, J. Magnet. Magnet. Mater. 293 (2005) 532–539, https://doi.org/10.1016/j.jmmm.2005.01.070.

[12] A. Roch, R.N. Muller, P. Gillis, Theory of proton relaxation induced by superparamagnetic particles, J. Chem. Phys. 110 (1999) 5403–5411.

[13] R.N. Muller, P. Gillis, F. Moiny, A. Roch, Transverse relaxivity of particulate MRI contrast media: From theories to experiments, Magnet. Resonan. Med. 22 (1991) 178–182, https://doi.org/10.1002/mrm.1910220203.

[14] C.V. Bowen, X. Zhang, G. Saab, P.J. Gareau, B.K. Rutt, Application of the static dephasing regime theory to superparamagnetic iron-oxide loaded cells, Magnet. Resonan. Med. 48 (2002) 52–61, https://doi.org/10.1002/mrm.10192.

[15] M.R.J. Carroll, R.C. Woodward, M.J. House, W.Y. Teoh, R. Amal, T.L. Hanley, T.G. St Pierre, Experimental validation of proton transverse relaxivity models for superparamagnetic nanoparticle MRI contrast agents, Nanotechnology 21 (2010), https://doi.org/10.1088/0957-4484/21/3/035103.

[16] R.A. Brooks, T2-shortening by strongly magnetized spheres: a chemical exchange model, Magnet. Resonan. Med. 47 (2002) 388–391, https://doi.org/10.1002/mrm.10064.

[17] M. Shinkai, H. Honda, T. Kobayashi, Preparation of fine magnetic particles and application for enzyme immobilization, Biocatal. Biotransform. 5 (1991) 61–69, https://doi.org/10.3109/10242429109014855.

[18] J. Mosafer, K. Abnous, M. Tafaghodi, H. Jafarzadeh, M. Ramezani, Preparation and characterization of uniform-sized PLGA nanospheres encapsulated with oleic acid-coated magnetic-Fe_3O_4 nanoparticles for simultaneous diagnostic and therapeutic applications, Coll. Surf. A: Physicochem. Eng. Aspect. 514 (2017) 146–154, https://doi.org/10.1016/j.colsurfa.2016.11.056.

[19] K. Bootdee, M. Nithitanakul, B.P. Grady, Synthesis and encapsulation of magnetite nanoparticles in PLGA: effect of amount of PLGA on characteristics of encapsulated nanoparticles, Polym. Bull. 69 (2012) 795–806, https://doi.org/10.1007/s00289-012-0773-3.

[20] S. Khalafalla, G. Reimers, Preparation of dilution-stable aqueous magnetic fluids, IEEE Trans. Magnet. 16 (1980) 178–183.

[21] N. Pernodet, M. Maaloum, B. Tinland, Pore size of agarose gels by atomic force microscopy, Electrophoresis 18 (1997) 55–58, https://doi.org/10.1002/elps.1150180111.

[22] American Society for Testing and Materials (ASTM) International, Standard Practice for Marking Medical Devices and Other Items for Safety in the Magnetic Resonance Environment, (n.d.). www.astm.org/Standards/F2503.htm.

[23] E. Pöselt, H. Kloust, U. Tromsdorf, M. Janschel, C. Hahn, C. Maßlo, H. Weller, Relaxivity optimization of a PEGylated iron-oxide-based negative magnetic resonance contrast agent for T_2 – weighted spin-echo imaging, ACS Nano 6 (2012) 1619–1624, https://doi.org/10.1021/nn204591r.

[24] P. Gillis, F. Moiny, R.A. Brooks, OnT2-shortening by strongly magnetized spheres: a partial refocusing model, Magnet. Resonan. Med. 47 (2002) 257–263, https://doi.org/10.1002/mrm.10059.

[25] A. Joos, N. Löwa, F. Wiekhorst, B. Gleich, A. Haase, Size-dependent MR relaxivities of magnetic nanoparticles, J. Magnet. Magnet. Mater. 427 (2017) 122–126, https://doi.org/10.1016/j.jmmm.2016.11.021.

[26] C. Paquet, H.W. de Haan, D.M. Leek, H.-Y. Lin, B. Xiang, G. Tian, A. Kell, B. Simard, Clusters of superparamagnetic iron oxide nanoparticles encapsulated in a hydrogel: a particle architecture generating a synergistic enhancement of the T $_2$ relaxation, ACS Nano 5 (2011) 3104–3112, https://doi.org/10.1021/nn2002272.

[27] F. Si-shen, S. Chong, J. Rompas, Chemotherapeutic Engineering: Collected Papers of Si-Shen Feng—a tribute to Shu Chien on His 82nd Birthday, CRC Press, 2014.

[28] H.B. Na, I.C. Song, T. Hyeon, Inorganic nanoparticles for MRI contrast agents, Adv. Mater. 21 (2009) 2133–2148, https://doi.org/10.1002/adma.200802366.

[29] A. Kostopoulou, A. Lappas, Colloidal magnetic nanocrystal clusters: variable length-scale interaction mechanisms, synergetic functionalities and technological advantages, Nanotechnol. Rev. 4 (2015), https://doi.org/10.1515/ntrev-2014-0034.

[30] F. Ludwig, T. Wawrzik, T. Yoshida, N. Gehrke, A. Briel, D. Eberbeck, M. Schilling, Optimization of magnetic nanoparticles for magnetic particle imaging, IEEE Trans. Magnet. 48 (2012) 3780–3783, https://doi.org/10.1109/TMAG.2012.2197601.

[31] D. Eberbeck, C.L. Dennis, N.F. Huls, K.L. Krycka, C. Gruttner, F. Westphal, Multicore magnetic nanoparticles for magnetic particle imaging, IEEE Trans. Magnet. 49 (2013) 269–274, https://doi.org/10.1109/TMAG.2012.2226438.

[32] N. Fatin-Rouge, K.J. Wilkinson, J. Buffle, Combining Small Angle Neutron Scattering (SANS) and Fluorescence Correlation Spectroscopy (FCS) measurements to relate diffusion in agarose gels to structure, J. Phys. Chem. B. 110 (2006) 20133–20142, https://doi.org/10.1021/jp060362e.

[33] A. Pluen, P.A. Netti, R.K. Jain, D.A. Berk, Diffusion of macromolecules in agarose gels: comparison of linear and globular configurations, Biophys. J. 77 (1999) 542–552.

[34] J. Narayanan, J.-Y. Xiong, X.-Y. Liu, Determination of agarose gel pore size: absorbance measurements vis a vis other techniques, J. Phys.: Conf. Ser. 28 (2006) 83–86, https://doi.org/10.1088/1742-6596/28/1/017.